

Wide Field Imaging of the Hubble Deep Field South Region II: The Evolution of Galaxy Clustering at $z < 1$ ¹

Harry I. Teplitz², Robert S. Hill³,
Eliot M. Malumuth³, Nicholas R. Collins³, Jonathan P. Gardner,
Povilas Palunas⁴, Bruce E. Woodgate

*Laboratory for Astronomy and Solar Physics, Code 681, Goddard Space Flight Center,
Greenbelt MD 20771*

Electronic mail: hit@binary.gsfc.nasa.gov,

ABSTRACT

We present the galaxy-galaxy angular correlations as a function of photometric redshift in a deep-wide galaxy survey centered on the Hubble Deep Field South. Images were obtained with the Big Throughput Camera on the Blanco 4m telescope at CTIO, of 1/2 square degree in broad-band $uBVR$ I, reaching ~ 24 mag. Approximately 40,000 galaxies are detected in the survey. We determine photometric redshifts using galaxy template fitting to the photometry. Monte Carlo simulations show that redshifts from these data should be reliable out to $z \sim 1$, where the 4000 Å break shifts into the I band. The inferred redshift distribution, $n(z)$, shows good agreement with the distribution of galaxies measured in the HDF North and the Canada-France Redshift Survey. After assigning galaxies to redshift bins with width $\Delta z = 0.33$, we determine the two point angular correlation function in each bin. We find that the amplitude of the correlation, A_w , drops across the three bins to redshift $z \sim 1$. Simple ϵ models of clustering evolution fit this result, with the best agreement for $\epsilon = 0$. Hierarchical cold-dark-matter models best fit in a low density, Λ -dominated universe.

Subject headings: cosmology: observations — galaxies: evolution – galaxies: clustering

¹Based on observations obtained at Cerro Tololo Inter-American Observatory, a division of the National Optical Astronomy Observatories, which is operated by the Association of Universities for Research in Astronomy, Inc. under cooperative agreement with the National Science Foundation.

²NOAO Research Associate

³Raytheon ITSS Corp., Lanham MD 20706

⁴Department of Physics, Catholic University of America, Washington DC 20064

1. Introduction

The Hubble Deep Field (Williams et al. 1996; HDFN) presented the deepest view of the universe in what is now the best studied 5 square arcminutes of the sky. With the addition of the Space Telescope Imaging Spectrograph (Woodgate et al. 1998; STIS) and the Near Infrared Camera and MultiObject Spectrometer (Thompson et al. 1998; NICMOS), the opportunity was presented to expand on the HDF program with an ambitious observation of the field around the $z=2.25$ QSO J2233-6033 (Boyle 1997). This Hubble Deep Field South (Williams et al. 2000; HDFS) provided a spectroscopic investigation of the matter along the line of sight to the QSO (Ferguson et al. 2000), the deepest image ever taken at optical wavelengths (Gardner et al. 2000), and deep optical and IR images of parallel fields (Casertano et al. 2000; Fruchter et al. 2000).

In 1997 September, we obtained broad-band $uBVRI$ imaging of half of a square degree around the HDFS. We have cataloged over 40,000 galaxies⁵. The first results from the project (Palunas et al. 2000a, hereafter Paper I) were a study of QSOs in this field. Here we present a measurement of the evolution of large-scale structure in the universe, using the angular correlations of galaxies as a function of photometric redshifts determined from our multi-color data. We will also publish the catalog in Palunas et al. (2000b; hereafter Paper III).

In the standard hierarchical model of galaxy formation and evolution, galaxy clustering traces overdense regions in the distribution of dark matter. High-redshift galaxies occur at the most extreme peaks in the density field and are thus biased tracers of mass—i.e., luminous matter is more strongly clustered than dark matter (Kaiser 1984). Subsequently, the clustering of the dark matter increases more rapidly than that of galaxies, so that the two distributions approach one another and are more similar today than in the past. In other words, the galaxy clustering bias is less. The way in which the bias decreases is a function of the cosmological parameters Ω , Λ , and $P(k)$ (e.g. Kauffman et al. 1999). Therefore, by measuring the evolution of the galaxy-galaxy correlation function, we can constrain models of structure formation.

Clustering has often been estimated from catalogues of two-dimensional sky coordinates of galaxies in order to infer the three-dimensional, physical correlation function, $\xi(r)$, using Limber’s equation (e.g., Peebles 1980). An important recent study of this type is the APM Galaxy Survey (Maddox et al. 1996). On the other hand, spectroscopic surveys have allowed direct measurement of $\xi(r)$ for local galaxies over a wide field (e.g. Lin et al. 1996). Studies at

⁵The data are publically available on the web at <http://hires.gsfc.nasa.gov/~research/hdfs-btc/>.

high redshift have had to rely on pencil-beam redshift surveys (e.g. Giavalisco et al. 1998) or wide-field photometric surveys in a single filter (Postman et al. 1998). Photometric redshifts now make it possible to combine the best of both techniques. While not accurate enough to determine $\xi(r)$, they are sufficient to assign the galaxies to redshift bins and study the evolution of $w(\theta)$ with redshift directly, rather than inferring the evolution from varying the magnitude limit (Connolly, Szalay, & Brunner 1998; Arnouts et al. 1999; Brunner, Szalay, & Connolly 2000). We have used this method to trace the evolution of clustering to $z=1$.

In section 2, we summarize the observations and data reduction. In section 3 we discuss the techniques used in the photometric redshift analysis. In section 4 we present the properties of the estimated redshifts. In section 5 we discuss the correlation of the cataloged galaxies as a function of redshift. We present our conclusions in section 6. Unless otherwise noted, a cosmology of $H_0 = 65 \text{ km s}^{-1} \text{ Mpc}^{-1}$, $\Omega_M = 0.3$, $\Omega_\Lambda = 0.7$ is assumed.

2. Observations

We obtained *uBVRI* imaging using the Big Throughput Camera (Wittman et al. 1998; BTC) on the Blanco 4-m telescope at CTIO. Observations were taken over three nights, 1998 September 16-18. Integration times and seeing conditions are listed in Table 1.

The BTC consists of four 2048×2048 pixel CCDs spaced in a grid, with a plate scale of $0.43''/\text{pixel}$. There are $5.4'$ wide gaps between the detectors, so it is necessary to observe in a dithered-grid pattern. The telescope was pointed at a grid of positions designed to fill in the gaps while maximizing the exposure time on a region around the HDFs quasar. We used 4 main positions spaced by $11.5'$. At each position, small offsets were made ($\sim 20''$) in order to measure the sky accurately in the object frames. The total area surveyed (to varying signal-to-noise ratio, SNR) was $2116 \square'$.

Initial data reduction is carried out using standard IRAF⁶ procedures and BTCPROC, a pipeline reduction package for BTC data (Wittman et al. 1998). The standard procedures include the usual CCD processing routines, such as bias subtraction, flat-fielding, and sky subtraction. The flat fields are created as “super-flats” from median combinations of all data taken throughout the night on a given chip in a given filter.

The large format BTC images have substantial optical distortions which affect the relative positions of objects, the plate scale, and the shapes of objects across the field of view. BTCPROC is designed to correct these distortions. First, a smoothed sky frame is subtracted

⁶IRAF is distributed by NOAO, which is operated by AURA Inc., under contract to the NSF

from each exposure (after the usual flat-fielding, etc.). Then, preliminary source catalogs for each image are created in BTCPROC using SExtractor (Bertin & Arnouts 1996). An initial geometric correction is applied to each catalog using an R -band astrometric solution provided by the BTC team (Wittman 1999; private communication). The catalog photometry is also corrected for variations in the plate scale. All of the preliminary catalogs are then matched to a fiducial position, in our case to the first R -band exposure, and a new astrometric solution is calculated for each image. The solution for each image is parameterized with four two-dimensional, cubic polynomials, one for each chip. An additional correction for geometric distortion in the shapes of objects is calculated to circularize the point spread function of stars selected from the catalogs.

The photometry from the initial catalogs is used to match the relative photometry between images and chips. Distortion corrected images are registered and then scaled by the photometry of stars in common. Finally, the registered, scaled images are combined by taking the median of each pixel value. The combined images are aligned (shifted and rotated) to J2000 coordinates, using astrometric observations of the HDFs field (Zacharias et al. 1998). We measure an RMS positional error of 0.07 arcseconds (0.16 pixels) in the astrometry of 223 stars.

A final catalog is constructed, again using SExtractor. In order to obtain color information through uniform apertures, objects are identified in each band and then measured on the same pixels in the other bands. For objects with strong R -band detections, that aperture is adopted for the photometry of the object; otherwise the highest SNR band is allowed to define the object.

The BTC data are observed through the Sloan u filter, the Johnson B and V filters, and the Cousins R and I filters. We fix our photometric system to that used by Landolt (1992); that is, Johnson UBV and Cousins RI . The photometry is calibrated using observations of the Landolt (1992) standard fields 95 and 113. Multiple stars are measured on each chip and photometric growth curves are constructed. Comparison of the Johnson and Sloan u filters demonstrates that small color corrections are sufficient to place our observations onto the same system as Landolt. Photometric errors are taken from the SExtractor catalogs. For use in this paper, all photometric data are converted from counts to flux density, f_λ , using the photometric zeropoints provided by Bessel (1990).

Star-galaxy separation is performed using the same method as in Paper I. Objects are classified based on their magnitude, FWHM, and SExtractor’s *class* parameter. Objects brighter than $R = 20$ are considered stars if they have $\text{FWHM} < 1.8''$ in the R -band. For objects with $20 < R \leq 23$, stars are defined as objects with $\text{FWHM}_R < 1.8''$ and $\text{class} > 0.95$. At faint magnitudes ($R > 23$), objects with $\text{FWHM}_R < 1.9''$ and $\text{class} > 0.92$ are classified as

stars. The classification is limited by the poor seeing of the observations ($FWHM = 1.75$ in the R -band); however, the star-galaxy separation is verified by comparing our classifications to those in the WFPC2 flanking fields (Lucas et al. 2000). For objects with $R < 24$, we find that the two data sets agree on the classification of 92% of the objects detected. The number of objects classified as stars is within $\sim 5\%$ of the prediction from Galactic star counts (Bahcall & Soneira 1981).

The catalog contains 53,657 objects with $V < 25.0$, of which 46,983 are classified as galaxies. For the photometric redshift analysis, we select the subset of the galaxies which are clearly detected (3σ) in BVR and either u or I , for a total of 29,023 galaxies.

3. Photometric Redshifts

Photometric redshifts have been successfully determined for many catalogs of galaxy photometry, most notably the HDFN observations (see Koo 1985, Brunner et al. 1997, Connolly et al. 1997, Lanzetta et al. 1996, Giallongo et al. 1998, Arnouts et al. 1999; Bolzonella et al. 2000; for a review see Hogg et al. 1998). The spectral energy distribution (SED) of a candidate galaxy is compared to a database of template spectra; the best fit between the two is considered to give the photometric redshift. The idea, while simple, depends on the complicated question of choosing the proper template spectra.

Lanzetta et al. (1996) have found that “redshifting” empirical spectra of four morphological types of local galaxies provides a sensitive means of fitting SEDs. The observed spectra adopted as input to their technique are those of Coleman, Wu & Weedman (1980; hereafter CWW). Brunner et al. (1997) prefer to use galaxy spectra actually measured at various redshifts as the template database. The limitation to that technique is the dearth of $1 < z < 2$ galaxy spectra available for comparison. Finally, many groups (e.g. Giallongo et al. 1998) have used the synthetic spectra of Bruzual & Charlot’s GISSEL96 models (see Bruzual & Charlot 1993) as templates. Although the advantage to synthetic spectra is the inclusion of evolution in the galaxy spectra, Lanzetta et al. argue that evolution mostly has the effect of moving the SED from one galaxy type to another.

We adopt the simplest of these approaches to fitting the photometric data. We compare the measured points to an “augmented CWW template set”, constructed from the CWW observed spectra and a single, bluer GISSEL96 model. The starburst model is taken from the GISSEL96 library with 0.5 Gyr age, solar metallicity, and a Salpeter IMF. The CWW spectra lack a blue starburst spectrum like the ones seen in (e.g.) the Kinney et al. (1993) library. We expect that the CWW spectra will better represent evolved, low-redshift galaxies than the

youngest high-redshift ones, which are often strikingly similar to low redshift starbursts (see Conti, Leitherer & Vacca 1996). Thus, we include CWW spectra for the likely low- z objects and a GISSEL96 starburst model spectrum for the likely high- z ones. A similar approach is taken by Gwyn et al. (1999), though they include more than one starburst. Following the usual approach to template selection, we do not include any AGN in the SEDs (but see Hatziminaoglou, Mathes, & Pello 2000). The contamination by AGN is expected to be very small. In 12 μm -selected samples, which are significantly less biased against finding Seyferts than our optically selected sample, only $\sim 7\%$ are spatially resolved AGN (Rush, Malkan, & Spinoglio 1993).

We now review the specifics of our technique. For all the template spectra, χ^2 is calculated over 102 redshifts. The redshift grid is evenly spaced in the square root of redshift. Other authors choose linearly or logarithmically spaced redshift points; however, we find that the square root is the best compromise to obtain sufficient coverage at both large and small redshifts.

The χ^2 test comparing the model SEDs to the observed photometric data is performed with the usual procedure. For each object observed,

$$\chi^2 = \sum_i \left[\frac{F_{O,i} - nc \cdot F_{T,i}}{\sigma_i} \right]^2,$$

where F_O is the observed flux for each filter i , with uncertainty σ_i , and F_T is the flux predicted by the template model spectrum. The template fluxes are normalized to the observed data by a constant, nc , which is determined (following Giallongo et al. 1998) to minimize χ^2 , such that $d\chi^2/dnc = 0$:

$$nc = \sum_i \left[\frac{F_{O,i} \cdot F_{T,i}}{\sigma_i^2} \right] / \sum_i \left[\frac{F_{T,i}^2}{\sigma_i^2} \right]$$

Given the varying sensitivity between filters, many objects are not detected in one or more bands. This problem is particularly evident in the u -band data, given the difficulty of obtaining good u -band photometry from the ground. In cases where no object is detected in a given filter, we use the measured flux from the region where the object is detected in other filters. Since our data are distortion corrected with a large set of astrometric positions, the registration should prevent this technique from introducing spuriously high flux from other objects (splitting of faint objects in such cases is handled by SExtractor).

The hundreds of χ^2 values form a surface, where the independent variables are the redshift and the galaxy template and the dependent variable is χ_ν^2 , the reduced χ^2 (see e.g. Bevington 1969). These surfaces typically contain 3-6 minima of varying depth. Each minimum corresponds to a photometric redshift for the object being tested. The most

likely inferred luminosity of each galaxy is favored: rather than simply eliminating the extreme solutions ($L_* < 0.001$ or $L_* > 10$), we form a weighting function, P_{LF} , by which we divide the χ^2_ν values. This function takes the form of a Schechter function (thus values near L_* are weighted highly, while the low luminosity end rolls off slowly, and the high luminosity end drops precipitously — see Figure 1). Specifically, $M_v^* = -21.5$ and $\alpha = -1.25$. This weighting function is not meant to represent the actual luminosity function of the galaxies, and no luminosity evolution is included. Rather P_{LF} is used to discriminate between extremely different minima in the common sense way that would be applied if each χ^2 -map were inspected by a person. Cases are rare in which multiple minima of substantially different redshift fall in the most probable ($P_{LF} > 0.5$) regime.

3.1. Calibration of the Photometric Redshift Technique

Accurate redshift estimation requires wavelength coverage of the strong spectral features. For example, at low redshifts the strongest feature is the 4000Å break. However, at $z > 1.2$ this break redshifts into the near-IR. As a result, many surveys (e.g. Connolly et al. 1997) have demonstrated the need for IR data to obtain accurate z_{phot} for the interesting $1 < z < 2.5$ era. At $z \sim 2.5$ the 912Å Lyman break redshifts into the blue end of the optical. The signal from this feature has led to the successful U - and B -band dropout technique (e.g. Steidel et al. 1996, Madau et al. 1996) of identifying Lyman break galaxies (hereafter LBGs) and the use of photometric redshifts to identify galaxies at $z \gtrsim 5$ (Lanzetta 1999).

In the case of the BTC data presented in this paper, we have $uBVRi$ photometry for all galaxies in the catalog. As a result, our analysis is limited to galaxies with $z_{phot} \leq 1$, where our spectral coverage is sufficient to detect the characteristic features.

To calibrate the accuracy of our procedure, we have created catalogs of simulated observations. The basis for these simulations is the GISSSEL96 models at a variety of ages, with solar metallicity. We expect that the dominant source of error in redshift recovery will be photometric noise, and so the effect of including non-solar metallicity input spectra to the simulations would be small. The GISSSEL96 input spectra sample galaxies from E through Sc as well as galaxies with strong starbursts. To obtain the simulated catalog, we randomly sample the distribution of spectroscopically measured redshifts for bright ($I_{AB} < 26$) galaxies in the HDFN and redshift the input spectra. This distribution is estimated using a smooth function fit to the HDFN data which have large gaps at $1 < z < 2$. Since our data are not deep enough to detect u -band dropouts, we only model galaxies up to $z = 3$. Simulated galaxies at $z > 2.5$ have Lyman forest blanketing applied using the decrements of Madau (1995). The redshifted spectra are scaled to a random sampling of HDFN I -band magni-

tudes, and random photometric error is added to each data point, within the expected error bars for our BTC data. Those objects with SNR sufficient for detection are retained in the simulated catalog.

Figure 2 shows the residual redshift error after applying our photometric redshift estimator to each simulated object. As expected, the $1 < z < 2$ regime is the most problematic for optical data, as the 4000Å break redshifts into the near IR, while the Lyman break is still in the ultraviolet. We find typical redshift errors at the 15-20% level for $z_{phot} < 1$. However, a number of $z_{spec} > 1$ galaxies are mis-identified as lower redshift objects. Table 2 shows the proportion of misidentified objects in several redshift ranges. This effect would be greatly reduced by adding IR observations. In the table, we list contamination of each bin by objects in bins that are not adjacent; that is, objects misidentified by the amount of the typical errors are not considered to be contamination, and some overlap at the boundaries of the bins is expected.

We also apply our photometric redshift procedure to two catalogs of spectroscopically confirmed galaxies. The first is the current set of HDFN galaxies, as tabulated by Fernandez-Soto et al. (1999). Figure 3 shows the comparison between our z_{phot} estimator applied to the HDFN WFPC2 data and the spectroscopic redshifts. Typical redshift residuals are $\Delta z \sim 0.1$ for $z < 1$. The lower residuals with this data are the result of more precise photometry.

The second spectroscopic data set is the catalog of AAT spectra for galaxies around the HDFs (Glazebrook et al. 2000; in preparation). More than 50 galaxies have spectroscopic redshifts. The objects in that catalog are in our field, so that a direct comparison with the BTC photometric redshift results is possible. Objects that are not resolved from neighbors or are severely contaminated from proximity to bright stars are discarded, leaving 31 galaxies. Of these, 19 have redshifts that Glazebrook et al. consider reliable; i.e., they have quality flags 3 or 4 which indicate greater than 50% probability for the redshift. Figure 4 shows the comparison with our inferred redshifts. Good agreement is found for most of the AAT sample, since it is restricted to $z < 1.2$.

Also in Figure 4, we compare our photometric redshift for objects in the HDFs WFPC2 field to estimates made from the HST data by Yahata et al. (2000) and Gwyn et al. (2000). Those groups agree to within $\Delta z \sim 0.2$ on the redshifts of ~ 40 galaxies in the WFPC2 field that we detect and resolve, and the comparison is made using those objects. Agreement is found within the errors between our estimates and theirs.

3.2. Errors in Photometric Redshifts

For the galaxy catalog, we have calculated the error in the redshift inferred for individual objects. These individual errors will not be used in the clustering analysis presented in this paper, but may be of interest in future work.

One common method of calculating the error on photometric redshift is to apply the standard $\Delta\chi^2 = 1$ statistic (e.g. Giallongo et al. 1998), i.e., the error, δ_z , is calculated by measuring the width in redshift of the χ^2 trough at the points where the value of $\chi_\nu^2 = (\chi_\nu^2)_{min} + 1$. This statistic produces good estimates of the error in z_{phot} as long as the minimum value of χ^2 is close to unity.

For many galaxies in our catalog, however the value of χ_ν^2 is significantly greater or smaller than one. Our simulations show that this is not an indication of insufficient resolution in the models; nor is it the result of systematic photometric errors (our extensive checks will be presented in Paper III). Accordingly, we adapt the $\Delta\chi^2 = 1$ method to our data by normalizing our χ^2 maps such that $(\chi_\nu^2)_{min} = 1$ before measuring the width of the $\Delta\chi^2 = 1$ trough. For galaxies having values of χ^2 near unity, this reverts to the usual method. The values we obtain for δ_z are consistent with the errors measured in our simulations (see Table 2 in Section 3.1). As expected, δ_z roughly increases with redshift and with photometric error.

4. Results

Figure 5 shows the number-redshift relation, $n(z)$ for the photometric redshifts of the galaxies in our catalog. Our result is compared to the distribution from Yahata et al. (2000) for the HDFs. The distribution of inferred redshifts agrees fairly well, although they see a sharp peak at $z \sim 0.5$ that is not present in our data. This may be the result of the small area over which their redshifts are estimated. Glazebrook et al. (2000; in preparation⁷) see evidence for a cluster at $z = 0.585$ in the WFPC2 field. The estimates of $n(z)$ by Yahata et al. (2000) are for a few hundred galaxies in the WFPC2 and NICMOS fields, and so could be biased by such a cluster. We also compare to the counts for photometric redshifts in the HDFN (Fernandez-Soto et al. 1999 and the references therein), and the spectroscopic redshifts from the Canada France Redshift Survey (Lilly et al. 1995). Our number-redshift counts show a good agreement with both samples out to $z = 1$.

⁷see <http://www.aao.gov.au/hdfs/Redshifts/>

The sample of galaxies for which we can fit redshifts is characterized by Figure 6. No brightness cut apart from that implicit in the fitting procedure is applied. The top row of plots shows histograms of SED type in each redshift bin, and the bottom row shows the distribution of M_R for each type. The distance modulus of each galaxy is computed using $\Omega_M = 0.3$ and $\Omega_\Lambda = 0.7$. The absolute magnitude is K-corrected using the best-fit SED. Also, a small correction is made for foreground extinction $E(B - V) = 0.027$ (Schlegel, Finkbeiner & Davis 1998). If the SED types are coded as successive integers, then the mean SED type, which is shown in the top row of plots as a short vertical line, moves very little between the z ranges. Fernandez-Soto et al. (1999) similarly find little evolution in the median galaxy type, although their type distribution is centered closer to the irregular galaxy model.

As expected for a magnitude-limited sample, the objects at high redshift are intrinsically brighter than those at low redshift for a given SED type. Thus, any derived quantities as a function of redshift may be affected by the implicit luminosity selection, and similarly for different apparent magnitude cuts. In the case of spatial correlation statistics, such effects are called luminosity bias (Park et al. 1994, Kauffmann et al. 1999).

In the highest-redshift bin, the distribution of best-fit SED types is peaked in the neighborhood of the mean type. An apparent deficit of E/S0 galaxies is especially conspicuous. This effect likely results from the combination of two factors: spectral evolution and a selection bias.

Spectral evolution affects the distribution of SED types at $z \sim 1$ because our small set of 5 SED templates is static, and each SED is labeled with the corresponding present-day galaxy type. Thus a young, rather blue galaxy at $z \sim 1$ that is fated to become a normal elliptical might be fit best by an SED appropriate to a present-day spiral. Accordingly, we expect that evolution will be reflected in the choice of template, resulting in a deficit of apparent E/S0 SED types at higher redshift. For the HDF-North, using a template set similar to ours, Fernandez-Soto et al. (1999) find that significantly more galaxies are matched by the bluer templates at higher redshifts, though they still do find some galaxies to be classified as E/S0. However, the HDF data include the near-infrared JHK passbands, whereas we are limited to the optical.

Selection bias may also affect the distribution of SED types. In order to fit a photometric redshift, we require a galaxy to be detected in at least 4 contiguous bands of the set $uBVRi$. Because the 4000 Å break at $z \sim 1$ is longward of the peak response in R , the rate of inclusion of red galaxies is expected to be less than that of blue galaxies. However, the SED type fitted for any galaxy in this redshift bin is also less meaningful than at lower redshifts because of relatively large photometric error in most of the bands. As a result, misclassification may contribute somewhat to the E/S0 deficit. The redshift itself is not affected either by this

ambiguity or by SED evolution, since it relies primarily on the location of the 4000 Å break.

5. Clustering Properties

5.1. Definitions

Our photometric redshift catalog can be used to examine the clustering evolution of galaxies at redshifts smaller than unity. With redshift uncertainties $\delta_z \sim 0.15$, physical clustering in three dimensions cannot be evaluated directly; instead, the angular correlation function is calculated for galaxies selected in redshift bins.

One measure of galaxy clustering is the spatial two-point correlation function ξ , which gives the excess probability of finding a galaxy at a given distance from another galaxy as compared to a uniformly random location. The expression for the joint probability of objects existing in two volume elements $\delta V_i, \delta V_j$ at a separation r is

$$\delta P = \mathcal{N}^2 [1 + \xi(r)] \delta V_i \delta V_j,$$

where \mathcal{N} is the mean space density of objects. If $\xi = 0$, then the objects are uniformly distributed. The clustering of objects on the sky is described by the analogous joint probability for angular separation,

$$\delta P = \mathcal{N}_\Omega^2 [1 + w(\theta)] \delta \Omega_i \delta \Omega_j,$$

where $w(\theta)$ is angular correlation function, $\delta \Omega_i, \delta \Omega_j$ are elements of solid angle, and \mathcal{N}_Ω is the mean surface density of objects. The angular correlation function is related to the spatial one by an integration over two lines of sight separated by angle θ , weighted with a selection function characterizing galaxy sampling as a function of distance. This integration is described by Limber's equation (Peebles 1980).

At low redshift and relatively small separations, ξ appears to be a power law,

$$\xi(r) = (r/r_0)^{-\gamma} \tag{1}$$

where r_0 is the correlation length, and γ is the slope. On scales smaller than $r = 10h^{-1}\text{Mpc}$, $\gamma \simeq 1.8$ and $r_0 \simeq 5h^{-1}\text{Mpc}$ (Groth & Peebles 1977; Davis & Peebles 1983; Tucker et al. 1997). If ξ is a power law, then so is $w(\theta)$. Specifically,

$$w(\theta) = A_w \theta^{-\delta}, \tag{2}$$

where $\delta = \gamma - 1$ (Peebles 1974).

The evolution of galaxy clustering with redshift may be parameterized as a power of $(1+z)$:

$$\xi(r, z) = (r/r_0)^{-\gamma}(1+z)^{-(3+\epsilon)}.$$

Clustering is fixed in comoving coordinates if $\epsilon = \gamma - 3$, and it is fixed in proper coordinates if $\epsilon = 0$. On the other hand, if $\epsilon > 0$, then clustering decreases in strength with lookback time, as expected from gravitational collapse. Baugh et al. (1999) roughly estimate that the prediction of linear perturbation theory, $\epsilon = +0.8$, approximately describes the clustering of dark matter, but that the ϵ model is not a good description of the clustering of galaxies. Angular correlations as a function of redshift can test this prediction. We evaluate $w(\theta)$ for our data grouped into redshift bins, and we compare this result to ϵ models integrated over the same redshift bins using Limber’s equation.

5.2. Estimation from Data

The magnitude of $w(\theta)$ is a measure of apparent clustering, i.e., of the departure of the galaxy sample from a random uniform distribution on the sky.

Several algorithms have been developed to estimate $w(\theta)$ from large data sets. We use a common method based on galaxy pair counts. Let θ_{ij} be the angular distance between galaxies i and j in the observed sample; then the distribution of all θ_{ij} normalized to a total of unity is called the data-data correlation (DD). Although DD is the fundamental observed distribution, it is not an estimator because of sampling biases. Two corrections are required: one for the geometry of the field and the other for the relationship between the observed galaxies and the edges of the field. These corrections are included through the random-random and data-random correlations (RR and DR, respectively), which are angular-distance distributions similar to DD. RR is computed from a random points distributed uniformly within the usable part of the observed field, and DR is computed from distances between observed and random points.

In this paper, we apply the estimator suggested by Landy & Szalay (1993),

$$w_{\text{LS}}(\theta) = \frac{\text{DD} - 2\text{DR} + \text{RR}}{\text{RR}}.$$

This estimator is preferred because its variance is approximately Poissonian, i.e., near the ideal minimum, and because it is unbiased in the weak correlation regime (Landy & Szalay 1993). This estimator is one of two that are in wide use currently. The other is the Hamilton (1993) estimator, which is symbolically described as $(\text{DD} \times \text{RR})/\text{DR}^2 - 1$. These estimators are compared analytically by Landy & Szalay (1993), and with Monte Carlo methods by

Kerscher, Szapudi, & Szalay (2000). Although there are slight differences between the two estimators, both are clearly superior to the alternatives. The Hamilton estimator has a subtle advantage in the three-dimensional analysis of flux-limited redshift surveys, whereas the Landy-Szalay estimator is less sensitive to the number of random points used in the computation. Therefore, the Landy-Szalay estimator is preferable for the present case.

The number of random points used to compute the RR and DR terms is chosen sufficiently large that the random error in w_{LS} is dominated by the DD term. The number of random points used to compute DR is not less than 100 times the number of galaxies in any given run. The RR term, which describes the geometry of the field irrespective of the galaxies, is computed separately using 16,000 iterations of 1000 random points apiece. For all the correlation runs, the field is masked to omit saturated stars, noise along the edges, and a few other noisy streaks or blemishes in the interior of the image (Figure 11, panel 0).

Implementation of the algorithm has been verified by processing the North Ecliptic Pole K -band catalogue used by Baugh et al. (1996) and reproducing their plot of $w(\theta)$. Verification has also been done using our data, by comparing $w_{\text{LS}}(\theta)$ to the “ensemble estimator”, $w_{\text{ens}}(\theta) = (\langle N_i - N \rangle \langle N_j - N \rangle) / N^2$, where N_i and N_j are counts in square cells 50 pixels ($21''.6$) on a side separated by angle θ , and N is the mean count over all such cells (Groth & Peebles 1977, Szapudi & Szalay 1998). The averages are taken over θ bins just as for pair-count estimates. These tests show that the $w_{\text{LS}}(\theta)$ algorithm is implemented correctly.

The value of $w(\theta)$ is modified by a correction for a bias due to the finite field size, called the integral constraint (IC). For a given form of $w(\theta)$, the ratio $c_A = \text{IC}/A_w$ depends on the field geometry. Assuming the power-law index $\delta = 0.8$, a Monte Carlo integration gives $c_A = 2.90$ for our field (θ in degrees). The correlation amplitude is calculated as the weighted average over bins of width $\Delta \log \theta = 0.2$ of $\tilde{A}_w(\theta) = w_{\text{LS}}(\theta) / (\theta^{-0.8} - c_A)$ for $\log \theta \in (-3, -0.2)$, equivalent to $\theta \in (3''.6, 0''.631)$. Similar procedures are used by Brainerd, Smail, & Mould (1995) and Villumsen, Freudling, & da Costa (1997).

Many correlation studies in the literature are based on one or two photometric bands, so that redshifts are not available. In these cases, samples are selected by faint magnitude limit, and generally, a decrease in correlation strength with the inclusion of more and fainter sources is found. Such samples can be selected from our database by ignoring the photometric redshift. Figure 7 shows our results for samples with $19 \leq R \leq 23$ and $19 \leq R \leq 24$, independent both of detection in other bands and of the success or failure of the redshift determination. The resulting estimates of the correlation strength A_w are shown together with those from several other studies. Although the values differ in detail among the various authors, our results are in good agreement with the consensus.

To study the evolution of the clustering strength with time, it is preferable to calculate the value of $w(\theta)$ as a function of redshift. To date, surveys relying on spectroscopic redshifts are hindered by small sample sizes or limited redshift range, so the approach of using photometric redshifts has recently been favored (Brunner et al. 1999; Arnouts et al. 1999). Adopting this approach, we divide our photometric redshift catalog into redshift bins and then examine the clustering strength in each bin. The size of the bin is an important issue (Arnouts et al. 1999). A bin size of $\Delta z = 0.33$ (twice the typical error) is adopted here in order to mitigate the contamination between adjacent bins.

Figure 8 shows $\log[w_{\text{LS}}(\theta) + \text{IC}]$ vs. $\log \theta$ for three redshift ranges covering $\Delta z = 0.33$ between z of 0 and 1, and for two different values of the faint R cutoff, 23 and 24. The error bars are discussed in Appendix A. The resulting estimates of correlation amplitude, assuming a fixed slope $\delta = +0.8$, are given as a function of redshift in Table 3 and Figure 9. The most obvious feature is an apparent decline in the correlation amplitude with redshift. The main focus of our error analysis is to assess the significance of this decline.

5.3. Clustering Evolution

The relativistic version of Limber’s equation in the narrow angle approximation (Phillips et al. 1978) is used to integrate the ϵ models over the redshift selection function $\phi(z)$. A functional form of ϕ appropriate for magnitude-limited catalogs is given by Efstathiou et al. (1991), such that ϕ has a single parameter, which is the median value of the argument z ; this ϕ has the shape roughly of a skewed Gaussian with a high- z tail. Villumsen et al. (1997) tabulate the median z as a function of limiting magnitude R_{max} ; their procedure is followed here. In Figure 7 we compare the models with values of A_{w} calculated from subsets of the BTC galaxies detected in R with magnitudes $19 \leq R \leq 23$ and $19 \leq R \leq 24$. The model with $\epsilon = +0.8$ agrees well with these results and is in general accord with similar results found in the literature.

The integrated ϵ models depend not only on the normalization to the present-day correlation length r_0 , but also on the adopted cosmological parameters. Figure 7 is plotted with $r_0 = 5.75h^{-1}$ Mpc, $\Omega_M = 0.3$, and $\Omega_\Lambda = 0.7$ (Baugh et al. 1999); however, the choice of $r_0 = 4h^{-1}$ Mpc, $\Omega_M = 1$, and $\Omega_\Lambda = 0$ (Villumsen et al. 1997) produces a virtually identical plot. In fact, in using Limber’s equation, r_0 , ϕ , and the cosmological parameters can be manipulated in concert to force a fit with a range of ϵ values over a substantial range of limiting magnitude. The influence of cosmological parameters on clustering history is explored by Kauffman et al. (1999).

Figure 9 shows the correlation amplitude A_w as a function of the photometric redshift bin. Again, the models are integrated using Limber’s equation. In this case, we assume a selection function ϕ with a simple form independent of galaxy brightness, i.e., a tophat of width $\Delta z = 0.33$ convolved with a Gaussian having $\sigma = 0.2$. The purpose of ϕ is to model the distribution of actual redshifts included in a given subset of galaxies. Here, the tophat is the redshift bin, and the Gaussian represents the random error in photometric redshift, which broadens the range of actual redshifts included. In contrast to Figure 7, the R -band apparent magnitude limit plays no role in the models in Figure 9, since the selection is made directly on the basis of observed redshift. Finer details of the distribution of actual redshifts within each photometric redshift bin represent higher-order effects that we do not attempt to model; moreover, the models intrinsically omit differential clustering biases such as luminosity bias.

In addition, we plot a galaxy formation model from Baugh et al. (1999) for $R < 23.5$ without dust obscuration. The Baugh et al. models in general show an upturn in clustering amplitude at $z \approx 1$. Both Baugh et al. (1999) and Arnouts et al. (1999) find observational support for this class of behavior. Our data do not extend to high enough redshift to see such an upturn; but at any rate, they are consistent with the model favored by Baugh et al. out to $z \sim 1$.

The clustering gives an appearance of marginally greater strength for the brighter galaxies in our measurements, suggestive of luminosity bias (Park et al. 1994; Kauffmann et al. 1999). This effect is not seen in the highest redshift bin; however, the errors on the $R < 23$ point are relatively large. Moreover, the models of Kauffman et al. (1999) show that luminosity bias itself evolves with z depending on how the luminosity cut is made. It is possible that the bias is less apparent at high redshift where the $R < 24$ cutoff is not faint enough to include the intrinsically fainter (less clustered) galaxies.

The apparent dearth of E/S0 galaxies in the highest-redshift bin (Figure 6) suggests that this bin may also be affected by a morphological clustering bias, such as that seen in the local universe (Hermit et al. 1996; Santiago & Strauss 1992; Giovanelli, Haynes, & Chincarini 1986; Davis & Geller 1976). The local bias is in the sense that early-type galaxies are more strongly clustered than late-type galaxies. Hence, if the highest-redshift bin is biased in favor of luminous galaxies and against E/S0 galaxies, then a morphological and a luminosity bias may work in opposite directions. However, any morphological effect appears to be diluted by its involving only $\sim 20\%$ of the galaxies, if the distribution of morphologies is extrapolated from that at $z < 0.67$. In any case, the highest redshift bin is naturally the one most subject to any such systematic effects and most in need of additional observations.

For the assumed cosmology and local clustering scales, the values of A_w that we measure

are best fit by $\epsilon = 0$ among all the ϵ curves, though they are also marginally consistent with the $\epsilon = 0.8$ case. The measurement for the middle bin ($0.33 < z < 0.67$) is more than 1σ below the $\epsilon = 0$ model, while the other data favor that model. Moreover, the shape of both $\epsilon \geq 0$ models is similar. Brunner et al. (1999) favor the $\epsilon = 0$ model in a study of clustering vs. photometric redshift for 3,000 galaxies over 0.054 square degrees. Their normalization is to $r_0 = 3h^{-1}$ Mpc, and their conclusion applies equally well to a universe with $\Omega_M = 1$ and to an open universe with $\Omega_M = 0.1$.

Most of the models shown in Figure 9 ($\epsilon \geq 0$, Baugh et al.) are no further than 2σ away from the data points, and so cannot be ruled out by these data alone. By contrast, Figure 7, which shows a similar plot for flux-limited samples, suggests that $\epsilon = +0.8$ is favored over the other models plotted. However, a detailed comparison between samples selected by photometric redshift and those selected solely by flux limit is probably not meaningful. The reason is that the clustering strength of the models is strongly affected by the integration over redshift (the depth dimension) via the assumed selection function $\phi(z)$. In turn, ϕ depends on the distribution of intrinsic galaxy luminosities and colors. Although we assume a standard form of ϕ for each of our two samples defined solely by flux limit (Efsthathiou et al. 1991), we have no independent check on the correctness of this assumption. Similarly, the true selection function for each of our photometric-redshift bins is also uncertain, as noted previously.

Our results for the two types of galaxy selection are consistent in that catalog subsets dominated by the lower redshifts show stronger clustering than those dominated by the higher redshifts. The sample defined solely by $R < 23$ (Figure 7) is more clustered than that defined solely by $R < 24$, and the sample defined by $z_{\text{phot}} < 0.33$ is more clustered than those with $z_{\text{phot}} > 0.33$. Furthermore, the selection functions adopted for integrating the clustering evolution models are at least roughly consistent with one another, since reasonable models yield correlation strengths in the range delineated by the observations for both types of catalog subsample.

Nevertheless, the primary purpose of fitting photometric redshifts is to be able to model $\phi(z)$ for a given subsample in a way that is both straightforward and independent of intrinsic galaxy properties. If the random error in photometric redshift is well characterized, then the actual selection function of a given sample should be better determined with this method than with a simple apparent magnitude cutoff. Accordingly, our expectation is that the model comparison in Figure 9 is more robust than that in Figure 7, to within the error bars.

The ability of studies like this one to discriminate between models of clustering evolution can be improved by increasing either the photometric depth or the sky area. Greater depth would provide a check for the present measurements both through improved photometry and

through an extension of the redshift range. A greater sky area would improve the precision of the clustering amplitude by increasing the number of galaxy pairs at every redshift.

6. Conclusions

Our data are consistent with a popular scenario for the evolution of clustering with redshift. As we noted above, more data will help distinguish between these cases.

Kauffmann et al. (1999) discuss the predictions of hierarchical CDM models on the observed clustering of galaxies. They explain that in a low density, Λ -dominated universe (Λ CDM), there is a “dip” (their phrasing) in the amplitude of galaxy clustering around $z \sim 1$. This dip occurs between the era of strong dark matter clustering traced by unbiased luminous galaxies (low redshift) and the era in which the observable galaxies are highly biased tracers of the densest (earliest clustered) regions. In a high density universe, the dip is absent, since structures form later and galaxies are more highly biased at higher redshifts; in that case, the clustering strength is constant for $z < 1$ and then rises sharply with redshift. CDM models also predict that the dip is weaker for redder, more luminous galaxies. Arnouts et al. (1999) demonstrate similar features in a wider array of CDM models, but with the same distinction between high density and low density universes. In our data, we find evidence for a decline out to $z \sim 1$, though the lack of higher redshift points prevents us from testing with our data alone whether this is a dip or an indication of a continuing decline. However, a reliable data point at $z \sim 3$ from the Lyman break galaxies (Giavalisco et al. 1998) suggests that a dip must occur somewhere in the intervening redshift range. The strength of this effect is magnified by the fact that at higher redshifts we appear to be seeing blue galaxies, for which the dip is expected to be stronger.

Our data are consistent with Λ CDM predictions for a low density universe. Although the strength of the evolution is debated, this scenario has been suggested by several studies (e.g. Postman et al. 1998, Le Fevre et al. 1996). Using the photometric redshift technique, Arnouts et al. (1999) find this kind of clustering evolution in the HDF (but note that Connolly et al. 1998 do not).

These results should be taken as a first look at the power of using the photometric redshift technique to measure clustering evolution on a sample of tens of thousands of galaxies on large scales. With the new instrumentation now becoming available on medium and large telescopes, this experiment will be repeated with higher accuracy out to larger redshifts. In particular, substantial improvements will occur when it is practical to obtain deep near-IR data over similar area.

We thank Hsiao-Wen Chen for a sanity check of the photometric calibration. This work was supported by the STIS Investigation Definition Team through the National Optical Astronomical Observatories and by the Goddard Space Flight Center.

A. Errors in the measurement of the angular correlation function

The sum in quadrature of random and systematic error in A_w is shown by the thin error bars in Figure 9, and the random error alone is shown by the thick error bars. By random error, we mean that arising from the galaxy counting statistics. Errors in $w(\theta)$ are Poissonian in the number of galaxy pairs in each θ bin (Peebles 1980, Landy & Szalay 1993); however, because θ bins are correlated, the naive least-squares error in the weighted average of $\tilde{A}_w(\theta)$ is incorrect. Rather than trying to find the covariance matrix of all the θ bins, a typical approach is to use a resampling method.

In general, resampling is similar to Monte Carlo methods, in that error is computed using artificial data sets drawn by chance; however, the data points are taken from the actual observations, rather than from an idealized model distribution. These samples are processed in the same way as the original data, and the standard deviation among all the answers is within a scale factor of the random error for the full observed data set.

A popular resampling method is the bootstrap (Efron & Tibshirani 1993; Barrow, Bhavsar & Sonoda 1984), in which each artificial data set is the same size as the observed data set. Necessarily, some data points are duplicated, while others are omitted. This process is the same as drawing the points from a pool consisting of an infinite number of replicas of the observed data (Diaconis & Efron 1983). However, its application to $w(\theta)$ is intuitively unsatisfying, because the duplicate galaxies are perfectly correlated. An analysis of the bootstrap for two-point correlation is given by Snethlage (1999), who finds that the resulting variances are too large.

Accordingly, we adopt an alternative resampling plan, based on the drawing of subsamples smaller than the original data set, without replacement; this method is known technically as the *delete-d jackknife*, where d is the number of points omitted to form each subsample (Efron & Tibshirani 1993). The jackknife is known in general to be applicable to a wider range of problems than the bootstrap (Davison & Hinkley 1997). Our argument for its use here is that each subsample represents a physically plausible distribution on the sky that is similar to the original, except sparser. The standard deviation of A_w fitted from multiple subsamples of a given size is scaled to the full number of data points, N , by multiplying by $N^{-0.5}$. In this case, $N \approx N_{\text{gal}}^2$ is the number of galaxy *pairs*, so that the error is scaled by

$$N_{\text{gal}}^{-1}.$$

The results of the delete- d jackknife are shown in Figure 10 for the 6 catalogue samples selected on R and z . Each closed circle represents 50 or 100 jackknife subsamples of the given size. The abscissa is the number of galaxies in each subsample, and the ordinate is the standard deviation of A_w computed only from the subsamples of that size. The line is an unweighted fit assuming the N_{gal}^{-1} scaling, and the open circle is the extrapolated error for the full number of galaxies. The closed triangles give upper and lower limits on the error in A_w ; the upper limit is the simple sum of the errors arising from individual θ bins, whereas the lower limit is the sum in quadrature. These limits represent the extreme cases of complete correlation (upper) and no correlation (lower) between θ bins. We adopt the extrapolated jackknife errors as the standard error in correlation amplitude, $\widehat{\text{se}}(A_w)$. These errors are ~ 2 times the respective lower limits (similar to the rule of thumb adopted by Baugh et al. 1996). For each of the two large samples selected on R magnitude only, the random error is extrapolated from one subsample containing 15% of the galaxies for $R < 24$ and 25% for $R < 23$.

Systematic as well as random error is assessed. One distinction between the two types of error is that the magnitude of systematic error can only be explored and not thoroughly characterized, whereas random error is a function of some reasonably well-understood distribution. Assessing systematic error involves anticipating possible problems that are not seen clearly in the measurements; for if the effects were well-defined, they could be corrected and relegated to the category of calibration.

Like random error, systematic error is estimated through a repeated computation of the correlation strength; however, in this case, the subsets of the original data are chosen deliberately rather than randomly. We take systematic error to be the result of additional structure imposed on the observed galaxy distribution by photometric non-uniformity. Two mechanisms are considered: (1) the dithering and the mosaicking of data from several chips, which result in variation by a factor of a few in effective exposure over the image; and (2) the possibility of insufficient masking around the 2 brightest stars, resulting in broad, low-amplitude clusters of noise spikes.

The subsets are chosen by masking out parts of the image. Figure 11 shows thumbnail images of the 9 masks used. Mask 0 is the standard R -band mask used to omit bright stars and edge effects. Mask 1 omits a range of columns in which is seen a modest concentration of galaxies that may be aligned with chip boundaries; masks 2 – 4 include only low, middle, and high ranges of total exposure, respectively; masks 5 – 7 are similar to 2 – 4, with extended masking around bright stars; and mask 8 includes the low and high ranges of total exposure, while omitting the middle range. The resulting values of A_w^{mask} for each masked

sample are plotted in Figure 12. The systematic error is computed for each range of z and R as $\delta_{\text{sys}}(A_w) = \sum N_m |A_w^{\text{mask}} - A_w| / \sum N_m$, where N_m is the number of galaxies included by each mask, and A_w has the same meaning as above, i.e., the adopted correlation strength as computed from the full sample. These errors are given in Table 3 and shown as a component of the error bars plotted in Figure 9.

If two outliers with small image area are ignored, the middle and high redshift bins are affected little by systematic error as defined above. However, the low-redshift bin shows a greater variation in correlation strength depending on field mask. This variation has a pattern: masks that mostly exclude a vertical stripe in the left half of the image, seen in panel 1 of Figure 11, give a relatively low correlation strength (panels 1,2,4,5,7, and 8 of Figure 11). The masks that mostly include this stripe give a consistent and relatively high correlation strength (panels 0, 3, and 6 of Figure 11). This region is selected by eye for special treatment in the error analysis because of a very subtle enhancement in galaxy surface density seen in certain visual displays, and because of a suspicion that this feature might be aligned with CCD chip boundaries in the final stacked image. However, the feature may also represent, in part, the real clustering signal that is sought. If the density enhancement is real, it is still too vaguely perceived to be analyzed as a distinct cluster.

REFERENCES

- Arnouts, S., Cristiani, S., Moscardini, L., Matarrese, S., Lucchin, F., Fontana, A. & Giallongo, E. 1999, MNRAS, 310, 540
- Bahcall & Soneira 1981, ApJS, 47, 357
- Barrow, J. D., Bhavsar, S. P., & Sonoda, D. H. 1984, MNRAS, 210, 19P
- Baugh, C. M., Gardner, J. P., Frenk, C. S., & Sharples, R. M. 1996, MNRAS, 283, 15
- Baugh, C. M., Benson, A. J., Cole, S., Frenk, C. S., & Lacey, C. G. 1999, MNRAS, 305, L21
- Bertin, E. & Arnouts, S. 1996, A&AS, 117, 393
- Bessell, M. S. 1990, PASP, 102, 1181
- Bevinton, P. R. 1969, *Data Reduction and Error Analysis for the Physical Sciences*, McGraw-Hill Book Company, New York, New York
- Bolzonella, M., Miralles, J.-M., & Pello, R. 2000, A&A, in press, astro-ph/0003380
- Boyle, B. 1997, AAONw, 83, 4
- Brainerd, T. G., Smail, I., & Mould, J. 1995, MNRAS, 275, 781

- Brunner, R. J., Connolly, A. J., Szalay, A. S. & Bershad, M. A., 1997, *ApJ*, 482, L21
- Brunner, R. J., Connolly, A. J., & Szalay, A. S. 1999, in "Photometric Redshifts and High Redshift Galaxies", eds. R. Weymann, L. Storrie-Lombardi, M. Sawicki & R. Brunner, (San Francisco: ASP Conference Series)
- Brunner, R. J., Szalay, A. S., & Connolly, A. J. 2000, *ApJ*, 541, 527
- Bruzual, A. G. & Charlot, S., 1993, *ApJ*, 405, 538
- Casertano, S., et al., 2000, *AJ*, in preparation
- Coleman, G. D., Wu, C. C., & Weedman, D. W. 1980, *ApJS*, 43, 393
- Connolly, A. J., Szalay, A. S., Dickinson, M., Subbarao, M. U., & Brunner, R. J. 1997, *ApJ*, 486, L11
- Connolly, A. J., Szalay, A. S., & Brunner, R. J. 1998, *ApJ*, 499, L125
- Conti, P. S., Leitherer, C., & Vacca, W. D. 1996, *ApJ*, 461, L87
- Davis, M., & Geller, M. 1976, *ApJ*, 208, 13
- Davis, M., & Peebles, P. J. E. 1983, *ApJ*, 267, 465
- Davison, A. C. & Hinkley, D. V. 1997, *Bootstrap methods and their application* (Cambridge: CUP)
- Diaconis, P. & Efron, B. 1983, *Scientific American*, 248, 116
- Efron, B. & Tibshirani, R. 1993, *An introduction to the bootstrap* (New York: Chapman & Hall)
- Efstathiou, G., Bernstein, G., Tyson, J. A., Katz, N., & Guhathakurta, P. 1991, *ApJ*, 380, L47
- Ferguson, H. C. et al. 2000, *AJ*, in preparation
- Fernandez-Soto, A., Lanzetta, K. M., & Yahil, A. 1999, *ApJ*, 513, 34
- Fruchter, A. S., et al. 2000, *AJ*, in preparation
- Gardner, J. P, et al. 2000, *AJ*, 119, 486
- Giallongo, E., D'Odorico, S., Fontana, A., Cristiani, S., Egami, E., Hu, E., & McMahon, R. G. 1998, *AJ*, 115, 2169
- Giallisco, M., Steidel, C. C., Adelberger, K. L., Dickinson, M. E., Pettini, M., & Kellogg, M. 1998, *ApJ*, 503, 543
- Giovanelli, R., Haynes, M. P., & Chincarini, G. 1986, *ApJ*, 300, 77
- Glazebrook, K. et al. 2000, in preparation

- Groth, E. J. & Peebles, P. J. E. 1977, *ApJ*, 217, 385
- Gwyn, S. D. J. 1999, in “Photometric Redshifts and High Redshift Galaxies”, eds. R. Weymann, L. Storrie-Lombardi, M. Sawicki & R. Brunner, (San Francisco: ASP Conference Series)
- Gwyn, S. D. J., et al. 2000, in preparation
- Hatziminaoglou, E., Mathez, G., & Pello, R. 2000, *A&A*, 359, 9
- Hermit, S., Santiago, B. X., Lahav, O., Strauss, M. A., Davis, M., Dressler, A., & Huchra, J. P. 1996, *MNRAS*, 283, 709
- Hogg, D. W. et al. 1998, *AJ*, 115, 1418
- Kaiser, N. 1984, *ApJ*, 284, 9
- Kauffmann, G., Colberg, J. M., Diaferio, A., & White, S. D. M. 1999, *MNRAS*, 307, 529
- Kerscher, M., Szapudi, I., & Szalay, A. S. 2000, *ApJL*, 535, L13
- Kinney, A. L., Bohlin, R. C., Calzetti, D., Panagia, N., & Wyse, R. F. G. 1993, *ApJS*, 86, 5
- Koo, D. C. 1985, *AJ*, 90, 418
- Landolt, A. U. 1992, *AJ*, 104, 340
- Landy, S. D. & Szalay, A. S. 1993, *ApJ*, 412, 64
- Lanzetta, K. M., Yahil, A., & Fernandez-Soto, A. 1996, *Nature*, 381, 759
- Lanzetta, K. M. 1999, *BAAS*, 195.1905
- Le Fevre, O., Hudon, D., Lilly, S.J., Crampton, D., Hammer, F., & Tresse, L. 1996, *ApJ*, 461, 534
- Lilly, S. J., Le Fevre, O., Crampton, D., Hammer, F., & Tresse, L. 1995, *ApJ*, 455, 50
- Lin, H., Kirshner, R. P., Shectman, S. A., Landy, D. S., Oemler, A., Tucker, D. L., & Schechter, P. L. 1996, *ApJ*, 471, 617
- Lucas, R. A. et al. 2000, *AJ* in preparation
- Madau, P. 1995, *ApJ*, 441, 18
- Madau, P., Ferguson, H. C., Dickinson, M. E., Giavalisco, M., Steidel, C. C., & Fruchter, A. 1996, *MNRAS*, 283, 1388
- Palunas, P., Collins, N. R., Gardner, J. P., Hill, R. S., Malumuth, E. M., Teplitz, H. I., Smette, A., Williger, G. M., Woodgate, B. E., & Heap, S. R. 2000a, *ApJ*, in press (Paper I)
- Palunas, P., et al. 2000b, in preparation (Paper III)

- Park, C., Vogeley, M. S., Geller, M. J., & Huchra 1994, *ApJ*, 569, 585
- Peebles, P. J. E. 1974, *A&A*, 32, 197
- Peebles, P. J. E. 1980, *The large-scale structure of the Universe*. Princeton University Press, Princeton
- Phillips, S., Fong, R., Fall, R. S., Ellis S. M., & MacGillivray, H. T. 1978, *MNRAS*, 182, 673
- Postman, M., Lauer, T. R., Szapudi, I., & Oegerle, W. 1998, *ApJ*, 506, 33
- Rush, B., Malkan, M.A., & Spinoglio, L. 1993, *ApJS*, 89, 1
- Sandage, A. 1997, *PASP*, 109, 1193
- Santiago, B. X. & Strauss, M. A. 1992, *ApJ*, 387, 9
- Schlegel, D. J., Finkbeiner, D. P, & Davis, M. 1998, *ApJ*, 500, 525
- Snethlage, M. 1999, *Metrika*, 49, 245
- Steidel, C. C., Giavalisco, M., Pettini, M., Dickinson, M., & Adelberger, K. L. 1996, *ApJ*, 462, L17
- Szapudi, S. & Szalay, A. S. 1998, *ApJLetters*, 494, 41
- Thompson, R. I., Rieke, M., Schneider, G., Hines, D. C., & Corbin, M. R. 1998, *ApJ*, 492, L95
- Tucker, D. L., et al. 1997, *MNRAS*, 285, 5
- Villumsen, J. V., Freudling W., da Costa, L. N. 1997, *ApJ*, 481, 578
- Wittman, D. M., Tyson, J. A., Bernstein, G. M., Lee, R. W., Dell’Antonio, I. P., Fischer, P., Smith, D. R., & Blouke, N. M. 1998, *Proc. SPIE*, 3355, 626
- Williams, R. E., et al. 1996, *AJ*, 112, 1335
- Williams, R. E., et al. 2000, *AJ*, in preparation
- Woodgate, B. E., et al. 1998, *PASP* 110, 1183
- Yahata, N., Lanzetta, K. M, Chen, H.-W., Fernandez-Soto, A., Pascarelle, S. M., Yahil, A., & Puetter, R. C. 2000, *ApJ* in press, (astro-ph/0003310)
- Zacharias, N., Corbin, T., Zacharias, M., Rafferty, T., Seidelmann, P. K., & Gauss, F. S. 1998, *BAAS*, 193.7509

Table 1. Observations

filter	exptime/frame	no. frames	seeing FWHM (")
<i>u</i>	1200	13	1.90
B	600	12	2.16
V	300	15	1.85
R	300	16	1.75
I	300	17	1.55

Table 2. Redshift Error Estimates from Simulations

z_{phot} range	mode $z_s - z_p$	σ_z	% contamination ^a
0–0.33	-0.01	0.12	3
0.33–0.67	0.01	0.16	3
0.67–1.00	-0.03	0.21	8
1.00–1.33	0.15	0.35	7
1.33–2.0	-0.41	0.58	40
2–3	1.1	0.72	68

^aobjects in z_{phot} bin whose true redshift belongs two or more bins away, for bins with $\Delta z = 1/3$; for example in the $0.33 < z < 0.67$ bin, nothing at $z < 1$ is contamination, but a $z_{true} = 1.2$ galaxy would be.

Table 3. Two-Point Correlation Results

Mag Limits	z Range	N_{gal}	A_w	$\widehat{\text{se}}(A_w)$	$\delta_{\text{sys}}(A_w)$
$19 \leq R \leq 23$	$0 - 0.33$	1423	5.45(-3)	6.8(-4)	1.9(-3)
	$0.33 - 0.67$	3992	2.92(-3)	2.0(-4)	3.6(-4)
	$0.67 - 1$	1842	1.96(-3)	3.4(-4)	6.4(-4)
$19 \leq R \leq 24$	$0 - 0.33$	2608	3.88(-3)	4.0(-4)	9.9(-4)
	$0.33 - 0.67$	6338	1.95(-3)	1.4(-4)	2.1(-4)
	$0.67 - 1$	3411	1.92(-3)	2.3(-4)	2.2(-4)
$19 \leq R \leq 23$	all	9467	1.37(-3)	1.0(-4)	...
$19 \leq R \leq 24$	all	22702	6.08(-4)	3.7(-5)	...

Fig. 1.— Values of χ^2 as a function of redshift for a typical galaxy (solid line). Each of the five galaxy templates produces a similar plot. For this galaxy, the late type spiral template (CWW) has the lowest value of χ^2 , and thus is shown here. The dotted line shows the redshift probability function, P_{LF} (normalized to unity at the maximum probability) for this $V=23.4$ galaxy. In this case, notice that it would clearly favor the lower redshift trough even if its χ^2 were slightly higher. The vertical dashed line shows the location of the χ^2 minimum, $z = 0.48$, and the horizontal dashed line shows the redshift error calculated by the width of the trough at the point at which χ^2 is double the minimum.

Fig. 2.— The error $\delta_z = z_{true} - z_{phot}$ in the photometric redshifts estimates for our simulated catalog of galaxies.

Fig. 3.— Our photometric redshifts, z_{phot} , are plotted versus spectroscopic redshifts, z_{spec} , for 100 galaxies in the HDF-north field. Our photometric redshifts are based on *UBVIJHK* photometry. The error bars shown were derived using a jackknife technique as described in Section 3.2. The dotted lines show a 0.2 deviation in the values.

Fig. 4.— z_{true} vs. z_{phot} for galaxies in the HDFS. Filled circles represent galaxies for which the spectroscopic redshifts are available from the AAT. Open diamonds represent galaxies without spectroscopic redshifts, but for which Gwynn et al. (1999) and Yahata et al. (2000) agree on photometric redshift within 0.2 in redshift. In both cases, only objects well separated from neighbors in our images are considered. Errors are calculated from the χ^2 distribution; see section 3.2.

Fig. 5.— The number-redshift relation, $n(z)$, for galaxies in our photometric redshift sample. Redshifts are counted in bins of width $\Delta z = 0.2$. $n(z)$ is also plotted for other photometric and spectroscopic redshift samples: the HDFN photometric redshifts (Fernandez-Soto et al. 1999); the spectroscopic redshifts of the CFRS; the photometric redshift for the HDFS of Yahata et al. (2000). Individual histograms are scaled to our $n(z)$ by the total number of objects in the sample.

Fig. 6.— Galaxy types as a function of redshift bin. The types are the best-fit SEDs from the photometric redshift computation, identified respectively with early-type galaxies (E/SO), spirals (Sbc, Scd), irregulars (Irr), and starbursts (StarB). Top panels: histograms of galaxy type in each photometric redshift bin; vertical line is mean galaxy type if types are coded as successive integers. Bottom panels: absolute R -band magnitude M_R (with K and evolutionary corrections); each galaxy is plotted as a dot; the box shows the quartile and median values of M_R for each SED type and redshift range.

Fig. 7.— Correlation strength vs. magnitude for R -magnitude limited galaxy samples.

Solid circles: galaxy samples from this work with $19 \leq R \leq 23$ and $19 \leq R \leq 24$; other symbols represent results from literature, extrapolated if necessary assuming that $w \propto \theta^{-0.8}$. Abscissa: R -band faint limit of apparent galaxy magnitude. Ordinate: correlation strength $A_w = w(1^\circ)$. Random error bars are smaller than the plotted points. Lines are models integrated using Limber’s equation with analytic selection function ϕ adopted from Villumsen et al. (1997) and assuming $\Omega_M = 0.3$, $\Omega_\Lambda = 0.7$, and $r_0 = 5.75h^{-1}$ Mpc. Dashed: $\epsilon = 1.6$; solid: $\epsilon = 0.8$; dotted: $\epsilon = 0$; dash-dot: Baugh et al. (1999) semi-analytic model for $R < 23.5$ and no dust.

Fig. 8.— Angular correlation functions for BTC-HDFS galaxies selected by apparent magnitude and redshift. Abscissa: log of angular separation θ in degrees. Ordinate: log of correlation function $w(\theta) + \text{IC}$, where IC is the integral constraint. Legends give magnitude and redshift ranges. Solid lines: best-fit functions of form $w = A_w \theta^{-0.8}$ (cf. Table 3); that is, the slope is fixed and only the fit is only for the amplitude.

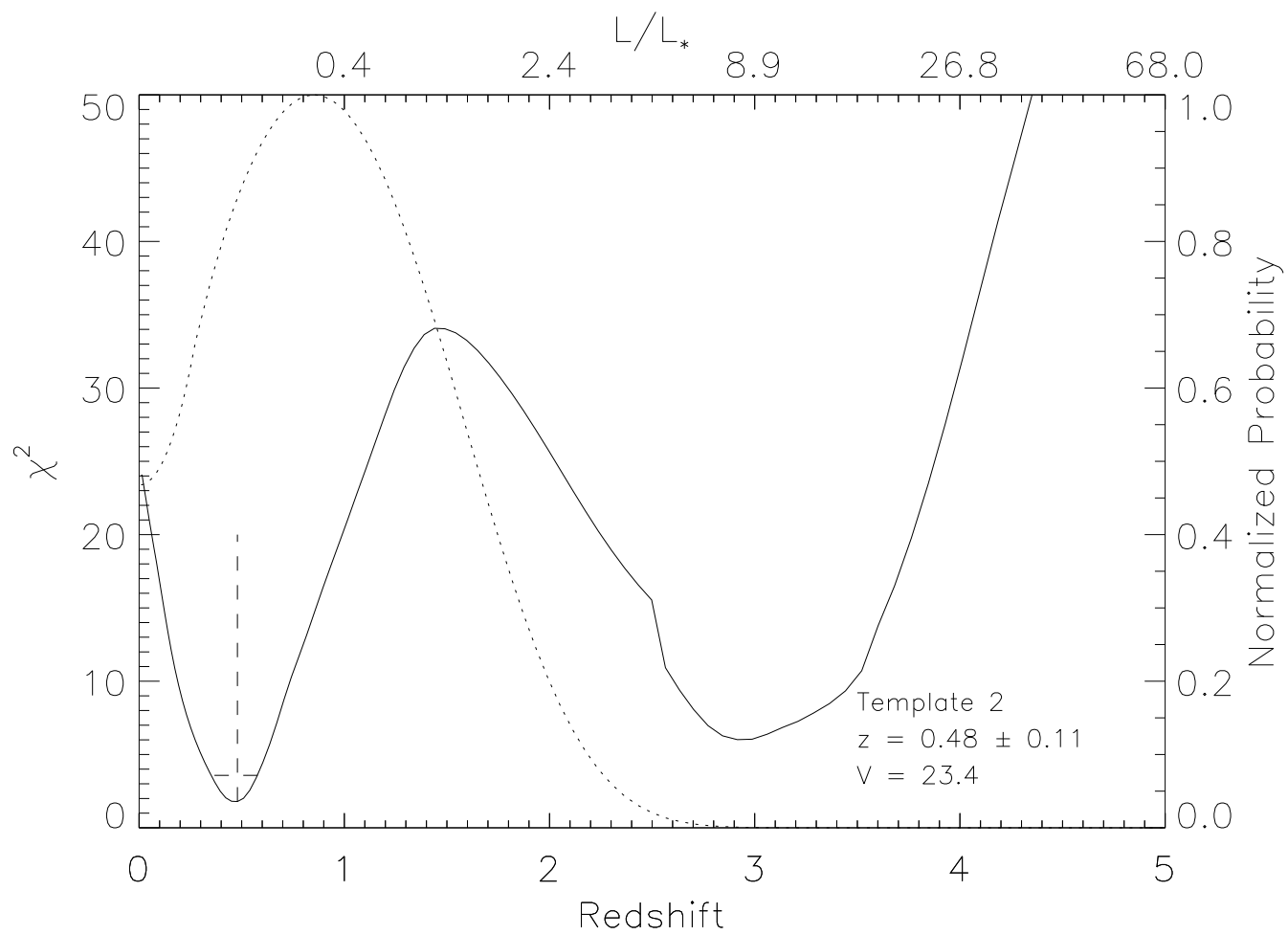
Fig. 9.— Correlation strength vs. redshift for samples with $19 \leq R \leq 23$ (squares) and $19 \leq R \leq 24$ (triangles). Abscissa: midpoint of redshift bin. Ordinate: correlation strength $A_w = w(1^\circ)$, assuming that $w \propto \theta^{-0.8}$. Thick error bars are random error arising from counting statistics of galaxies. Thin error bars are sum in quadrature of random error and an estimate of systematic error resulting from variation in sensitivity over R -band image. Lines are models of galaxy evolution for $\Omega_M = 0.3$, $\Omega_\Lambda = 0.7$, and $r_0 = 5.75h^{-1}$ Mpc. Models are integrated using Limber’s equation; the selection function ϕ is a tophat of width $\Delta z = 0.33$ convolved with a Gaussian of $\sigma(z) = 0.2$. Solid: $\epsilon = 0.8$; dotted: $\epsilon = 0$; dash-dot: Baugh et al. (1999) semi-analytic model for $R < 23.5$ and no dust; dash-triple dot: $\epsilon = -1.2$.

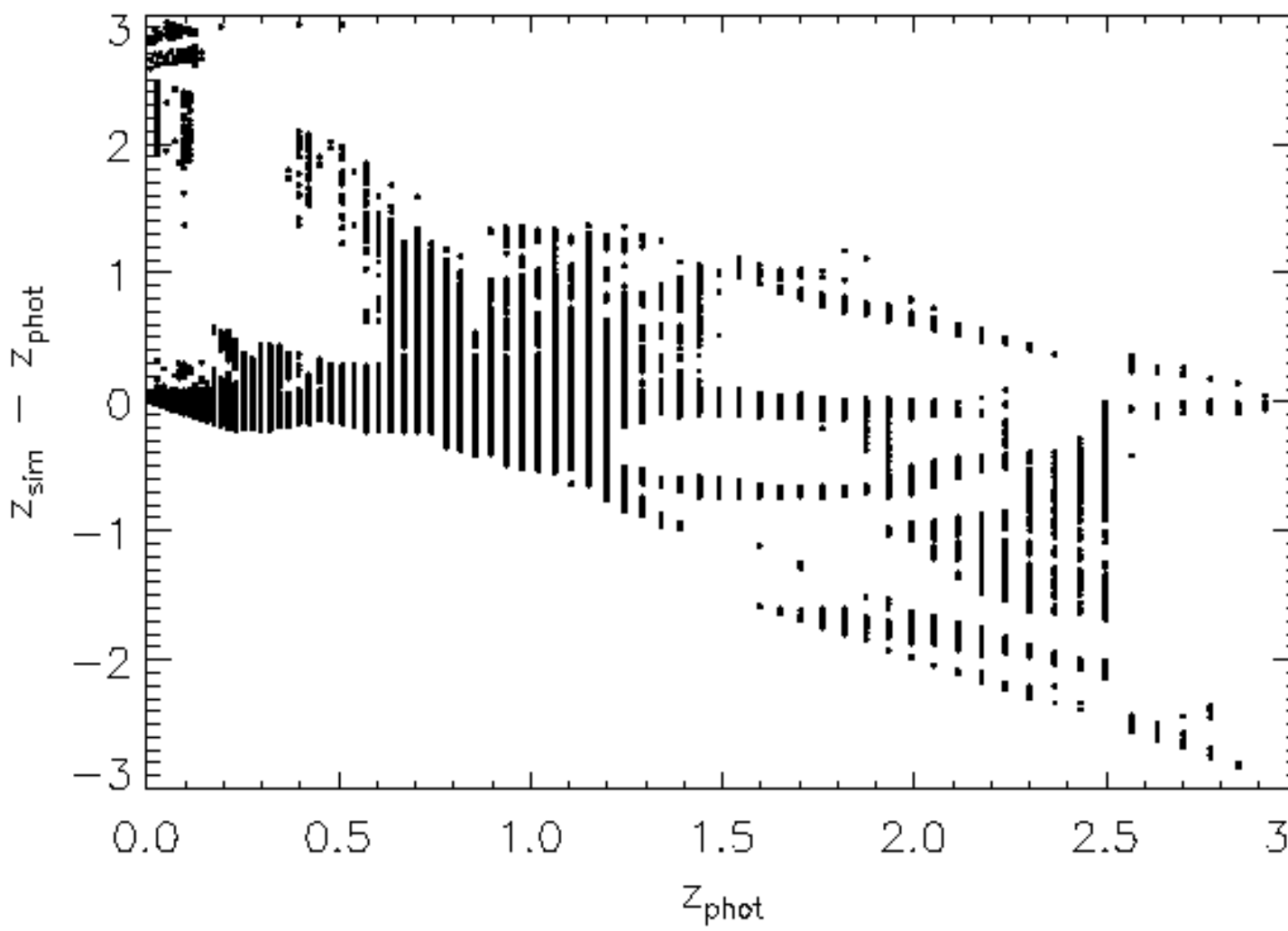
Fig. 10.— Random errors in A_w obtained from delete- d jackknife. Each panel is for a given R magnitude and redshift range, as indicated by the legends, and each point is a particular subsample or extrapolated value. Abscissa: number of galaxies in subsample. Ordinate: standard deviation in A_w among 50 or 100 subsamples of the given size. Jackknife results are given by solid circles, and open circles show the extrapolation to the full galaxy sample. Triangles show upper and lower limits on error assuming that the various angular (θ) bins in the DD correlation are perfectly correlated (top triangle) and perfectly independent (bottom triangle), respectively.

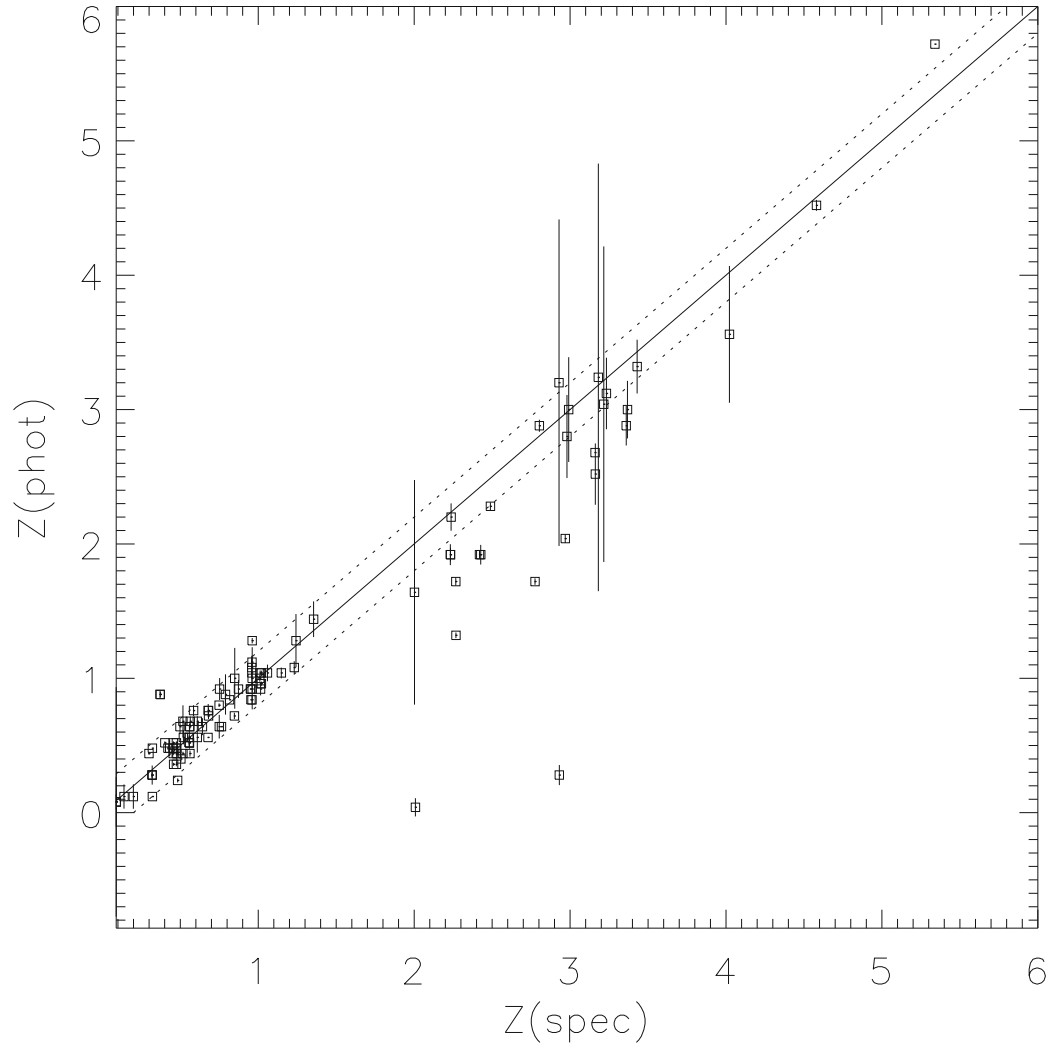
Fig. 11.— Masks for R -band BTC image used in correlation computations and systematic error assessment. Black areas are excluded, and white are included. The SNR (or total exposure) over the frame is divided for this purpose into three ranges, low, medium, and high (cf. Figure 12). Top row, left: default mask, which excludes saturated stars and blemishes;

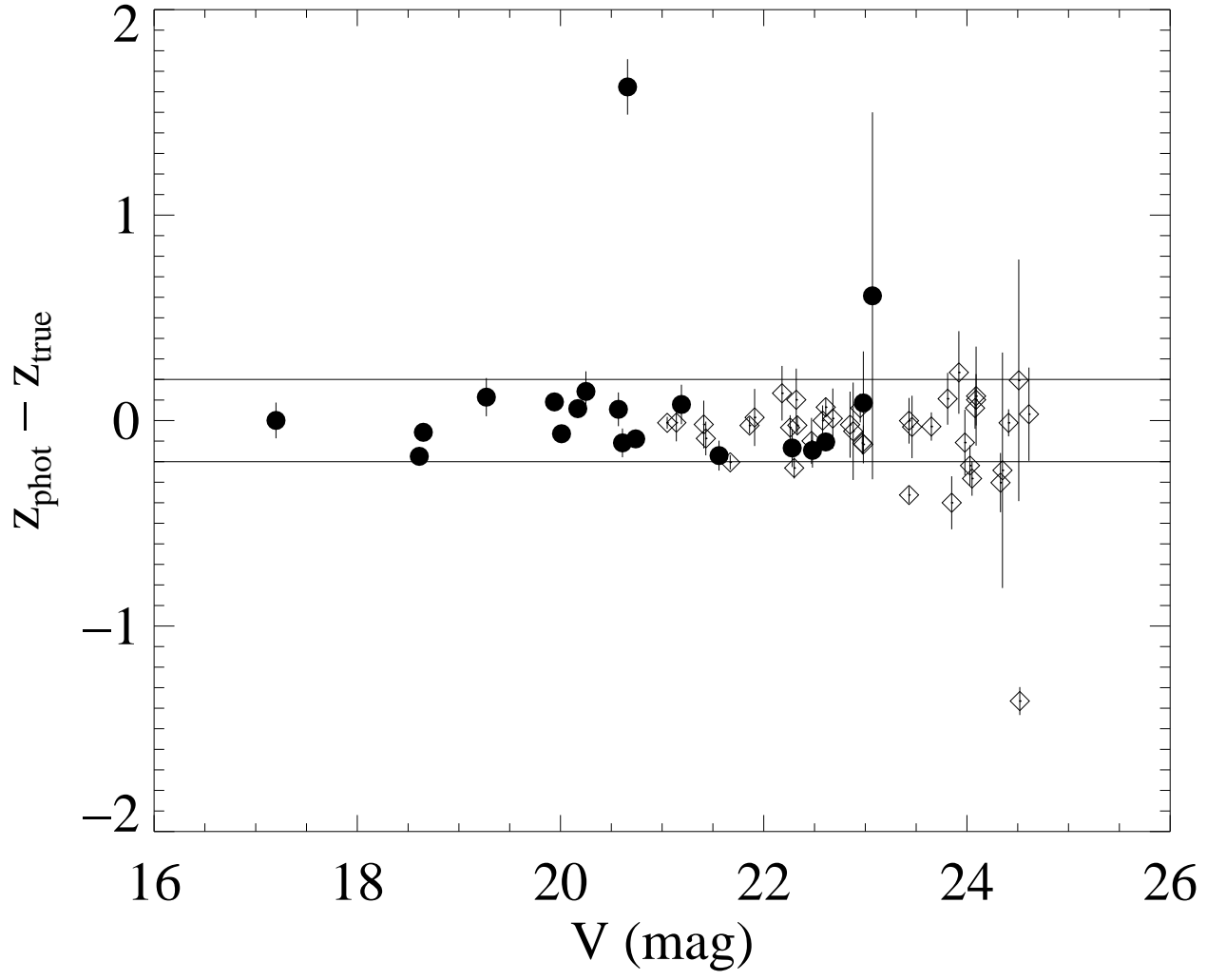
center: vertical stripe containing possible low-level galaxy surface density enhancement excluded; right: only areas of low SNR included. Middle row, left: only areas of medium SNR included; center: only areas of high SNR included; right: low SNR included, with extra masking around two bright stars. Bottom row, left: medium SNR included, with extra masking around two bright stars; center: high SNR included, with additional masking around two bright stars; right: areas of both low and high SNR included.

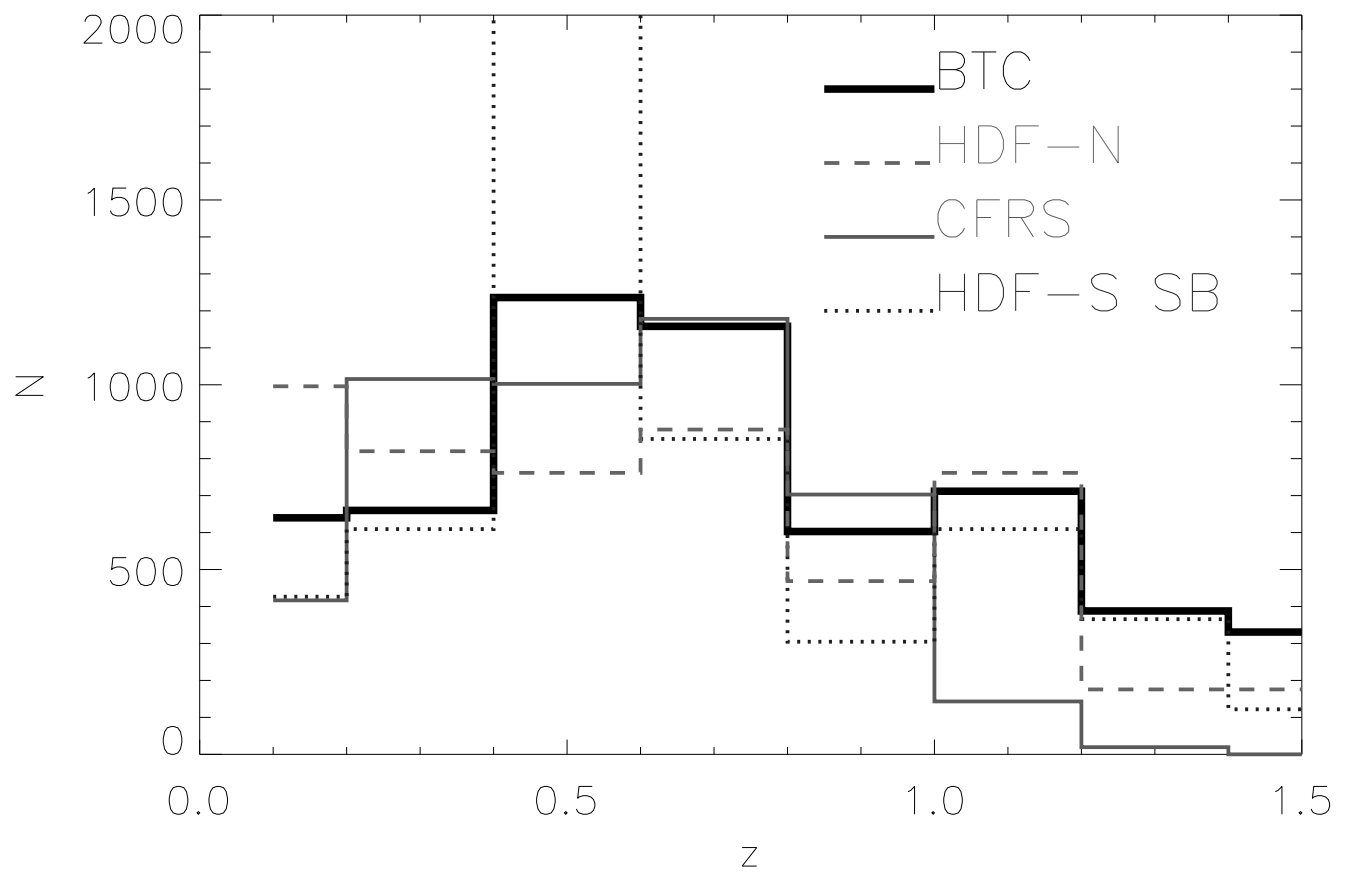
Fig. 12.— Variation in correlation strength as a result of varying sensitivity over the R -band image. Abscissa: mid-point of redshift bin; actual values are 0.167, 0.5, and 0.833, but symbols are shifted for clarity. Ordinate: correlation strength $A_w = w(1^\circ)$ for subsample masked as shown in Figure 11. Legend describes masks and gives proportion of sources admitted by each. The lowest redshift bin shows the greatest variation apart from outliers. Estimator w_{LS} used with 2.5×10^5 random points in each DR run, and 1000 iterations of 1000 points in each RR run; integral constraint computed for each mask with 1000 iterations of 1000 random points.

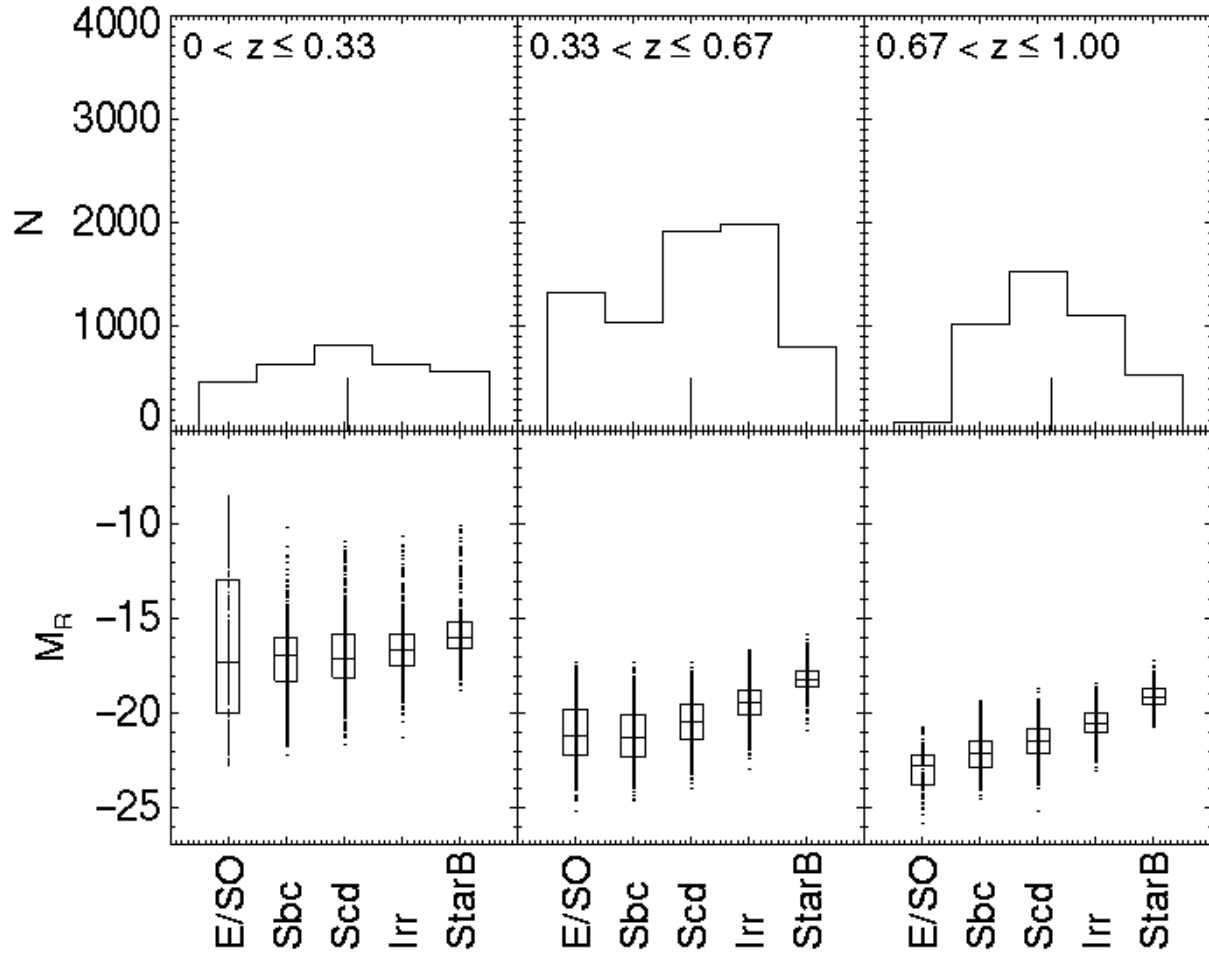


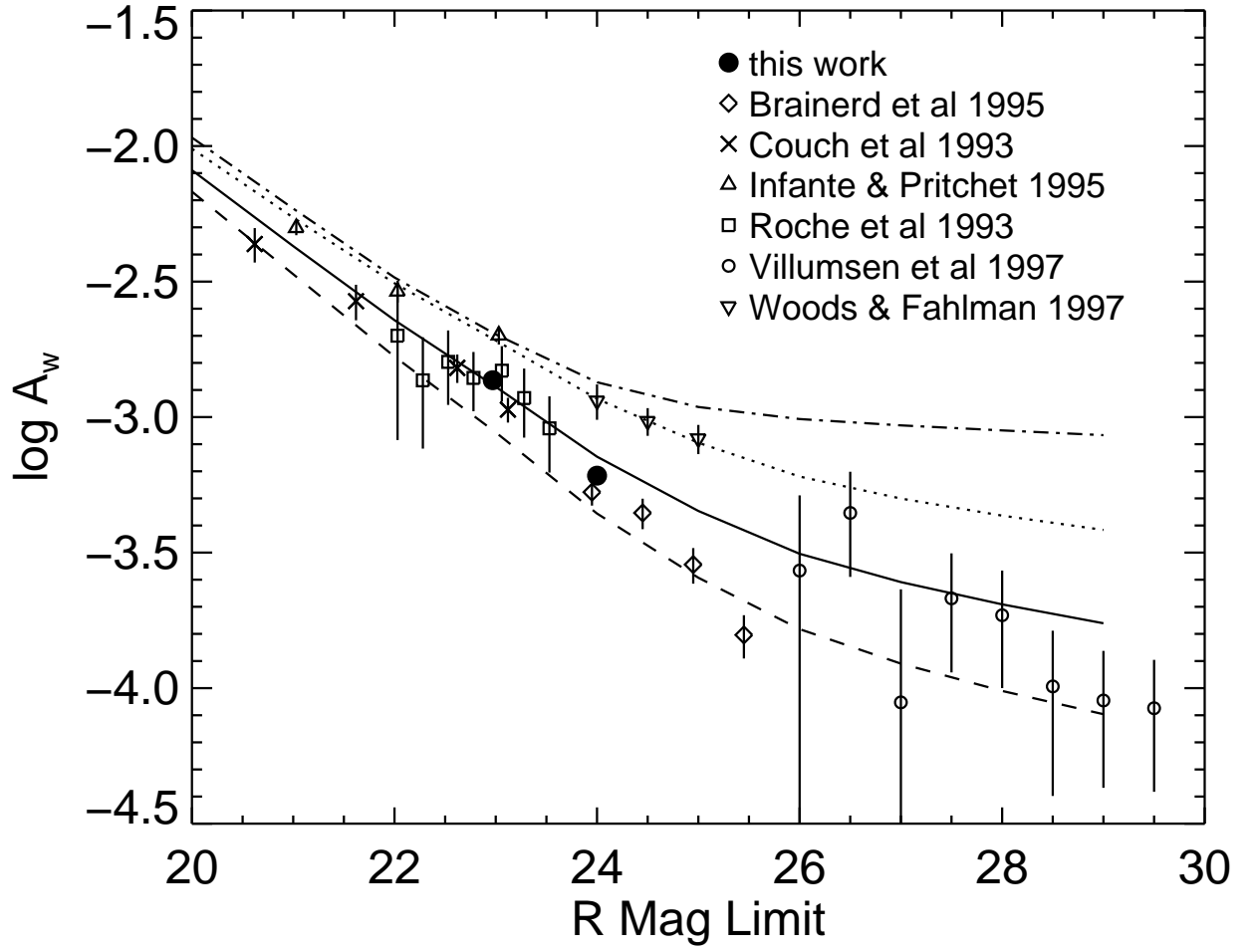


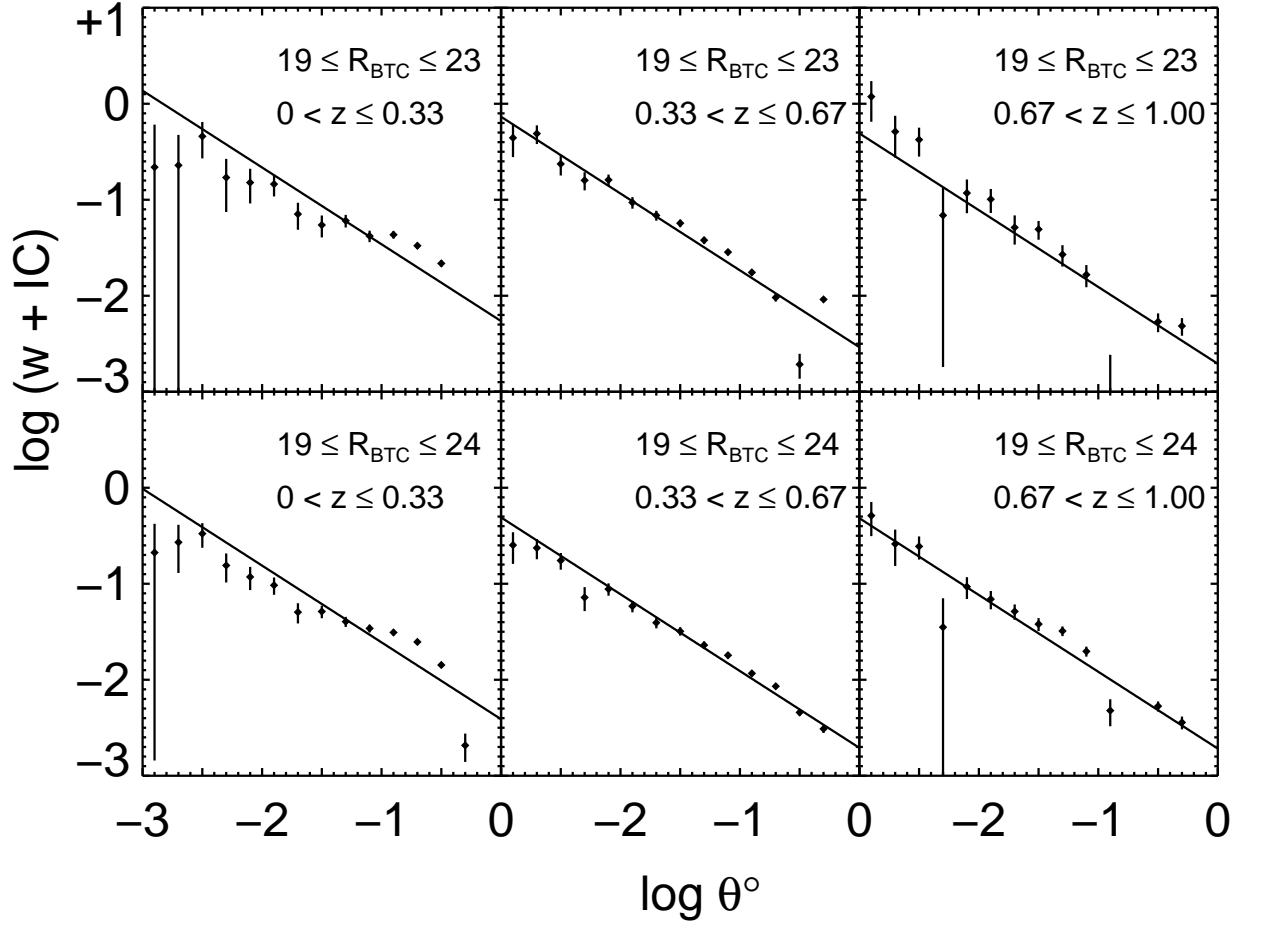


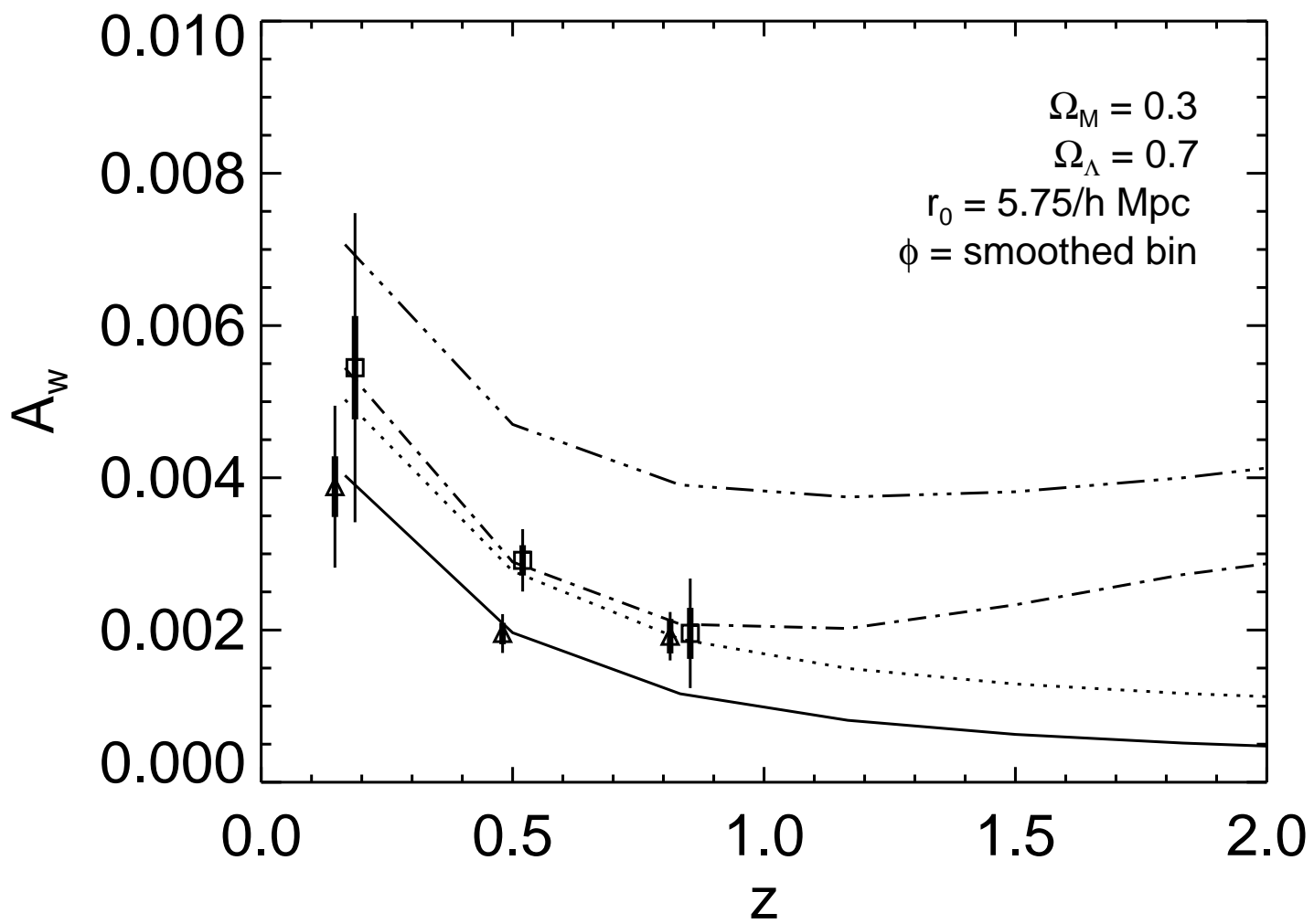


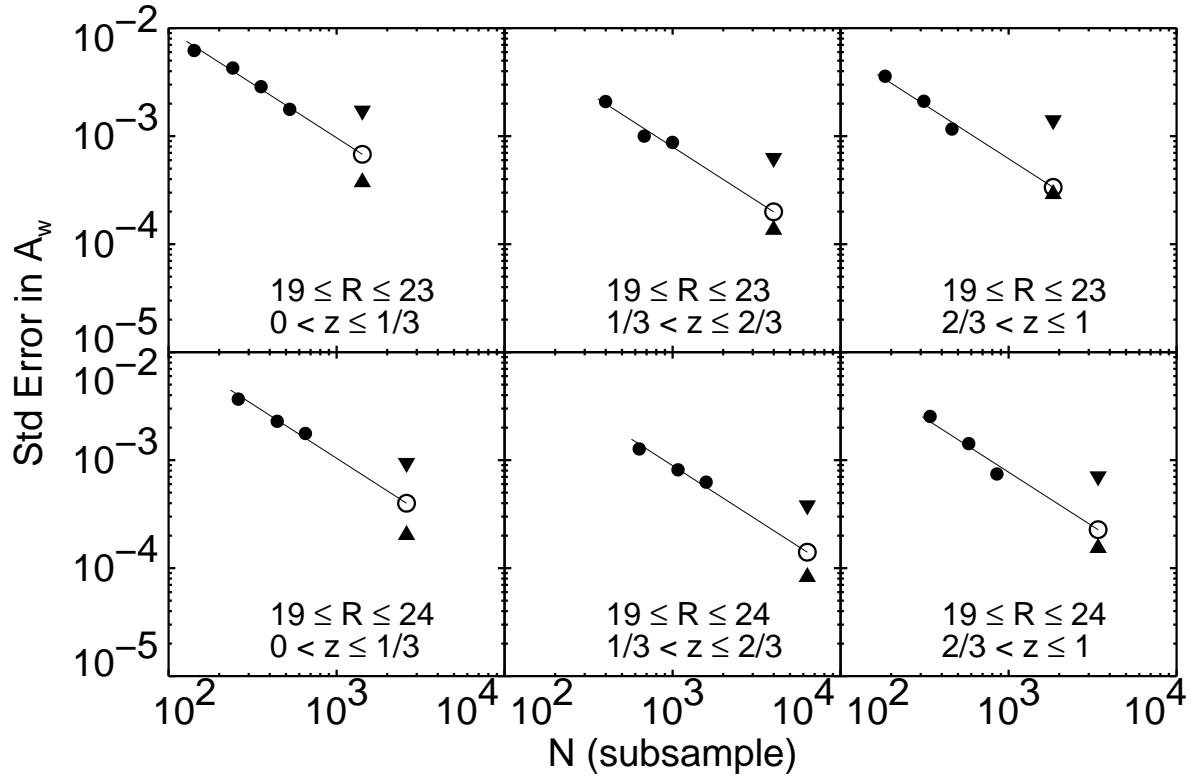










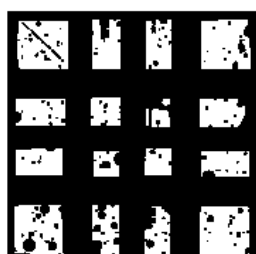




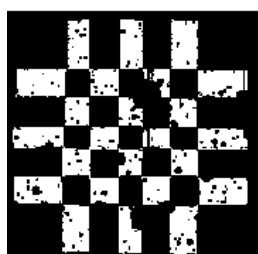
STANDARD



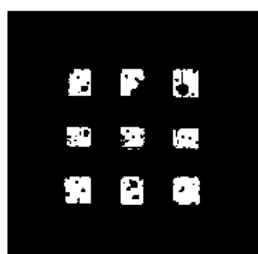
STRIPE



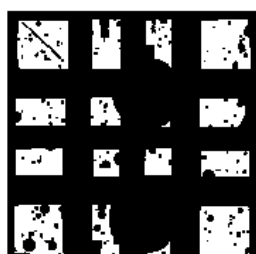
LOW EXPOS



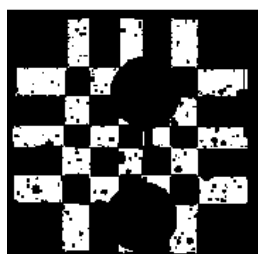
MID EXPOS



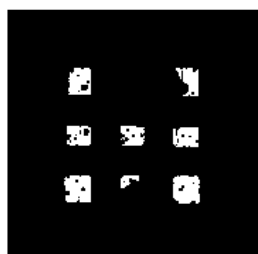
HIGH EXPOS



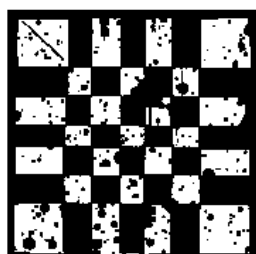
LOW EXPOS-EXTRA



MID EXPOS-EXTRA



HIGH EXPOS-EXTRA



LOW + HIGH EXPOS

